

Atmospheric effects of stellar cosmic rays on Earth-like exoplanets orbiting M-dwarfs

F. Tabataba-Vakili^{1,2}, J. L. Grenfell³, J.-M. Grießmeier^{4,5}, and H. Rauer^{1,3}

¹ Zentrum für Astronomie und Astrophysik, Technische Universität Berlin, Hardenbergstraße 36, 10623 Berlin, Germany

² Now at: Atmospheric, Oceanic and Planetary Physics, Department of Physics, University of Oxford, Oxford OX1 3PU, UK e-mail: Fachreddin.Tabataba-Vakili@physics.ox.ac.uk

³ Institut für Planetenforschung, Deutsches Zentrum für Luft- und Raumfahrt, Rutherfordstraße 2, 12489 Berlin, Germany

⁴ Laboratoire de Physique et Chimie de l'Environnement et de l'Espace, Université d'Orléans / Centre National d'Etudes Spatiales, France

⁵ Station de Radioastronomie de Nancay, Observatoire de Paris - Centre National d'Etudes Spatiales/Institut national des sciences de l'Univers, USR 704 - Université Orléans, Observatoire des Sciences de l'Univers en région Centre, route de Souesmes, 18330 Nancay, France

December 22, 2021

ABSTRACT

M-dwarf stars are generally considered favourable for rocky planet detection. However, such planets may be subject to extreme conditions due to possible high stellar activity. The goal of this work is to determine the potential effect of stellar cosmic rays on key atmospheric species of Earth-like planets orbiting in the habitable zone of M-dwarf stars and show corresponding changes in the planetary spectra. We build upon the cosmic rays model scheme of Grenfell et al. (2012), who considered cosmic ray induced NO_x production, by adding further cosmic ray induced production mechanisms (e.g. for HO_x) and introducing primary protons of a wider energy range (16 MeV - 0.5 TeV). Previous studies suggested that planets in the habitable zone that are subject to strong flaring conditions have high atmospheric methane concentrations, while their ozone biosignature is completely destroyed. Our current study shows, however, that adding cosmic ray induced HO_x production can cause a decrease in atmospheric methane abundance of up to 80%. Furthermore, the cosmic ray induced HO_x molecules react with NO_x to produce HNO₃, which produces strong HNO₃ signals in the theoretical spectra and reduces NO_x-induced catalytic destruction of ozone so that more than 25% of the ozone column remains. Hence, an ozone signal remains visible in the theoretical spectrum (albeit with a weaker intensity) when incorporating the new cosmic ray induced NO_x and HO_x schemes, even for a constantly flaring M-star case. We also find that HNO₃ levels may be high enough to be potentially detectable. Since ozone concentrations, which act as the key shield against harmful UV radiation, are affected by cosmic rays via NO_x-induced catalytic destruction of ozone, the impact of stellar cosmic rays on surface UV fluxes is also studied.

Key words. Astrobiology, cosmic rays, Planets and satellites: atmospheres, Planets and satellites: terrestrial planets, radiative transfer, photochemistry, ozone, methane

1. Introduction

With the discovery of the first exoplanet around a main-sequence star (Mayor & Queloz 1995), the scope of the search for life has extended beyond our solar system. As of today, nearly 2000 exoplanets have been detected, over 1200 of these via the transit method, in which the occultation of the star by the planet can be measured photometrically.¹ Transiting exoplanets are of interest for the detection of life, since it is theoretically possible to characterise their atmosphere spectroscopically for sufficiently bright targets. This would allow the detection of chemical compounds that are associated with life forms, termed biosignatures.

Water plays a crucial role in the development and sustenance of life as we know it. This has led to the concept of the habitable zone (HZ; see Huang 1959; Kasting et al. 1993). The HZ is defined as the orbital distance range of the planet where its surface may maintain water in liquid form. This range depends e.g. on the planet's atmospheric composition and the temperature of its host star. Herein lies one advantage of the comparatively cool M-dwarf host stars: habitable planets are situated closer to

their host, which improves the geometric probability of a transit. Other favourable characteristics of M-dwarf hosts include their small size, which improves detectability of Earth-sized planets in the HZ, and the large abundance of M-dwarf stars in our Galactic vicinity (Scalo et al. 2007).

Since a habitable planet orbiting an M-dwarf star lies so close to its host and because the planet might have a weak magnetosphere (due to tidal-locking), the planet may be subject to high particle fluxes (Grießmeier et al. 2005), which are termed cosmic rays (CRs). These CRs are categorised by origin: Galactic cosmic rays (GCRs) originate outside the Solar System, while solar (or stellar) cosmic rays (SCRs) originate from the Sun (or the host star of the studied planet). Independent of their origin, CRs can interact with the planetary atmosphere, possibly destroying important biosignature species or affecting the radiative balance of the atmosphere by destroying key radiative species.

For Earth, extensive research has gone into understanding the ionizing effects of SCRs and solar proton events on the chemistry of middle atmosphere (e.g. Jackman et al. 1990, 2005; Winkler et al. 2008). In this region CRs are one of the key chemical forcing mechanisms. On the other hand, GCRs provide a constant forcing on the atmospheric chemistry over all altitudes.

¹ see <http://exoplanet.eu/>

Nicolet (1975) and Solomon et al. (1981) have studied the rate of CR-induced NO_x and HO_x production. Recently, Calisto et al. (2011) have analysed the effect of GCRs on the global atmospheric chemistry with a 3D chemistry-climate model. They suggest that on Earth GCRs can locally produce up to 30% of available NO, causing a loss of up to 3% in the ozone column.

Owing to their favourable detection criteria (Scalo et al. 2007), the habitability of M-dwarf planets has been extensively studied. For instance, dynamical three-dimensional studies suggest that tidally-locked planets, which are expected to be common in the HZ of M-dwarfs, have regions that may be able to sustain habitable conditions (Joshi 2003). Exoplanet parameter studies using GCMs focus largely on quantifying the effect of certain parameters on the planet's habitability and general circulation. These vary for instance the orbital eccentricity (Dressing et al. 2010), the planetary obliquity (Spiegel et al. 2009), the surface roughness (Rauscher & Menou 2012), or the stellar spectrum (Godolt 2012). Further recent GCM studies, e.g. by Yang et al. (2013), propose that clouds on tidally-locked exoplanets provide a stabilizing feedback, expanding the M-dwarf habitable zone. Studies of atmospheric loss processes (e.g. Lammer et al. 2011) suggest that planets with nitrogen-rich atmospheres orbiting M-dwarfs may be eroded during the early stages of planetary evolution unless the planet was protected by a strong intrinsic magnetic field.

The detectability of biosignatures in M-dwarf planet atmospheres is directly linked to the planet's atmospheric chemistry. Key studies that address biosignature detectability (e.g. Selsis 2000; Selsis et al. 2002; Des Marais et al. 2002; Segura et al. 2003, 2005; Tinetti et al. 2006; Ehrenreich et al. 2006; Kaltenegger et al. 2007; Kaltenegger & Traub 2009; Kaltenegger & Sasselov 2010; Rauer et al. 2011; Tessenyi et al. 2013) investigate the impact of varying e.g. the stellar spectrum, the abundance of radiative species, or background atmospheres on synthetic emission and transmission spectra of hypothetical exoplanets.

With regard to the photochemistry of exoplanets orbiting M-dwarfs, Segura et al. (2005) studied the effect of M-class stellar spectra on the atmospheric chemistry, which suggested strongly increased atmospheric concentrations of CH₄ and H₂O with the assumption of an Earth-like atmosphere (i.e. N₂, O₂ dominated, 1 bar surface pressure). A recent study by Tian et al. (2014) suggested that abiotic production of O₂ from CO₂ photolysis could be significant for planets orbiting M-dwarf stars. Grenfell et al. (2007a) investigated the effect of GCRs on biomarker molecules for biogenic Earth-like planets surrounding an active M-dwarf with varying heliospheric and planetary magnetic shielding. This study was recently built on by Grießmeier et al. (2015b) and Grießmeier et al. (2015a), who use the updated version of the CR model presented in the current work to examine the effect of the planetary magnetospheric shielding on GCR-induced photochemistry. With a maximum of 20% difference in column-integrated ozone values (and 6% for CH₄ and H₂O) between no magnetic shielding and ten times the Earth's magnetic field strength, they find GCRs have nearly no effect on the resulting planetary spectra. A further study by Grenfell et al. (2012) focused on the effect of high-intensity SCR fluxes on the atmospheric chemistry via the mechanism of CR-induced NO production. They concluded that SCRs are able to significantly reduce the O₃ column by 99.99% for highly flaring stars via NO_x-induced catalytic destruction.

This work focuses on the photochemical response to stellar cosmic rays and the corresponding effects upon theoretical planetary spectra and surface UV radiation of an Earth-like planet

orbiting an M-dwarf star. The main aim of the current study is to improve upon the cosmic ray modelling scheme provided by Grenfell et al. (2012), thereby expanding the energy range of incident particles and adding further CR-induced photochemical mechanisms (NO_x and HO_x production). The improved model is then used to provide new insights into the biomarker chemistry of Earth-like exoplanets. We then study the effect of changes in the atmospheric chemistry on the spectral signals of key biosignature species, and evaluate surface UV fluxes.

The UV flux on the planetary surface can have harmful consequences to life forms and therefore affects the habitability of a planet. The UV surface flux is strongly affected by the interplay of top of atmosphere (TOA) fluxes and atmospheric O₃ concentrations. Segura et al. (2010) have modelled the photochemical effects of a large UV flare observed on AD Leonis (AD Leo), and find that UV surface fluxes stay within non-lethal dosages. Grießmeier et al. (2015b) find that GCR-induced O₃ destruction results in up to 40% increased biologically weighted UV surface flux. However, as the AD Leo spectrum used features lower UV-A and UV-B fluxes and the planetary atmosphere retains enough O₃ to shield from UV-C, total UV fluxes are much lower than on Earth. When using the flaring UV spectrum of Segura et al. (2010) for both "long" and "short" flare scenarios, Grießmeier et al. (2015b) find that the GCR-induced O₃ reduction would not be harmful to life with maximum biologically weighted UV surface fluxes not exceeding four-times Earth values. Grießmeier et al. (2015b) used a similar model version as this work i.e. without time dependence. "Long" flares were assumed to maintain the atmosphere in a continuously perturbed state, whereas for "short" flares it was assumed that the atmosphere did not respond photochemically. Grenfell et al. (2012) suggests that for planets in the HZ of M-dwarfs, the effect of SCRs to atmospheric O₃ concentrations is more devastating and can cause nearly full atmospheric transmissivity of UVB radiation. The addition of new CR-induced photochemical mechanisms in the current work has a significant effect on O₃ concentrations and hence has an effect on UV fluxes. Consequently, we evaluate the effect of SCRs to biologically weighted UV surface fluxes using the scenarios presented in Grießmeier et al. (2015b).

This paper is organised as follows: Section 2 describes the models used. The model scenarios are introduced in Section 2.1. In Section 2.2 the radiative-convective/photochemical model is described. The improvements introduced to the cosmic ray scheme are detailed in Section 2.3. Results regarding atmospheric changes due to the incident SCRs are presented in Sect. 3.1. In Sect. 3.2 significant chemical mechanisms are identified. The resulting planetary emission and transmission spectra are presented in Sect. 3.3. In Sect. 4 the UV flux at the planet's surface is investigated. Sections 5 and 6 provide a discussion and concluding remarks.

2. Model description

Analogous to Grenfell et al. (2012), we first compute the primary cosmic ray proton flux at TOA from measurements of the CR flux of the Sun outside the Earth's magnetic field. For the Earth reference, we use a GCR particle spectrum and we assume an Earth-equivalent magnetic field and shielding using the magnetospheric model of Grießmeier et al. (2005, 2009). For the M-dwarf cases we assume a planet without magnetic field shielding, which gives an upper limit to the effect of the CR flux. The SCR flux is scaled quadratically with distance to the HZ of the M-dwarf (see Sect. 2.1), and is then input into the TOA of the photochemical part of our 1D radiative convective photochem-

istry model (see Sect. 2.2), where an air-shower approach using a Gaisser-Hillas scheme (see Grenfell et al. 2007a) is applied to calculate secondary electron fluxes (see Sect. 2.3). Contrary to Grenfell et al. (2012) who only calculate NO molecules from these electron fluxes, we additionally introduce CR-induced NO_x (N, NO) and HO_x (H, OH) production using parametrisations of the ion pair production rate (IPR) found in Jackman et al. (2005) and Solomon et al. (1981), respectively (see Sect. 2.3.1). The converged steady-state solution of the atmospheric model is then inserted into a spectral line-by-line model called SQUIRRL (Schreier & Schimpf 2001; Schreier & Böttger 2003) to calculate theoretical emission and transmission spectra (see Sect. 2.4).

2.1. Cosmic ray spectra and model scenarios

Similar to Grenfell et al. (2012), we look at a number of scenarios, ranging from a planet without CRs to a planet exposed to a flaring M-dwarf star. For the M-star cases, the planet is positioned at a distance of 0.153 AU to its host star such that the total irradiance received by the planet is equal to one solar constant. For the stellar spectrum of the host we use the well-studied spectrum of AD Leonis (AD Leo), which is a strongly flaring M-type star, to provide comparison to previous works. A discussion of the effects of different host spectra can be found in Sect. 5.

Little is known about the SCR fluxes of M-dwarf stars. Khodachenko et al. (2012) (their section 2) summarise current uncertainties. Most studies that investigate the effects of SCRs upon Earth-like atmospheres therefore use solar values for the stellar wind parameters (e.g. Grenfell et al. 2012; Segura et al. 2010). More recently, 3D Magnetohydrodynamic (MHD) models have been applied to estimate stellar winds on M-dwarfs and their interaction with the planetary magnetosphere (see e.g. Vidotto et al. 2013, 2015), which suggest a strong particle output for active M-dwarf stars.

0. **Earth reference case:** For the reference case, we use the Galactic cosmic ray reference spectrum outside the magnetosphere given by Seo et al. (1994). The cosmic ray flux at the top of the atmosphere is calculated by numerically simulating the transport of these particles through an Earth equivalent magnetosphere using the magnetospheric model described in Griebmeier et al. (2005); Grenfell et al. (2007a); Griebmeier et al. (2015a).
1. **M-dwarf w/o CR:** In this case, CRs are absent.
2. **quiescent M-dwarf:** This case is based on the SCR proton spectrum measured at solar minimum, using the cosmic ray spectrum of Kuznetsov et al. (2005) at 1 AU (their Fig. 2, solid line). No shielding by a planetary magnetic field is assumed.
3. **active M-dwarf:** This case is based on the SCR proton spectrum measured at solar maximum, using the cosmic ray spectrum of Kuznetsov et al. (2005) at 1 AU (their Fig. 2, dashed line). No shielding by a planetary magnetic field is assumed.
4. **flaring M-dwarf:** This case is based on the SCR proton spectrum measured during the September 30, 1989 solar proton event, using data measured at 1 AU by the spacecrafts GOES 6 and 7 (Smart & Shea 2002, their Fig. 11). No shielding by a planetary magnetic field is assumed.

For the Earth reference case, we use a solar input spectrum based on Gueymard (2004). The M-dwarf spectrum of AD Leo is produced from observations in the UV by the IUE satellite, in the visible by Pettersen & Hawley (1989), and in the near-IR by Leggett et al. (1996). For wavelengths longer than 2.4 μm , data

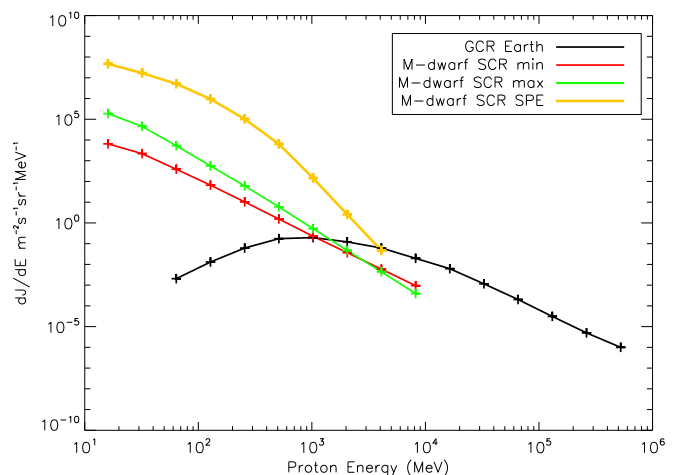


Fig. 1. Cosmic ray proton flux spectra at top of atmosphere. Solar cosmic ray spectra for quiescent (case 2, red line), active (case 3, green line), and flaring (case 4, yellow line) M-dwarf scenarios (without planetary magnetic shielding) were scaled to 0.153 AU. The black line shows the average Galactic cosmic ray spectrum for Earth at 1 AU (case 0).

from a model by Hauschildt et al. (1999) was used. Apart from this all modelled scenarios are Earth-like as presented in Sect. 2.2

For scenarios 2, 3, and 4, we convert the measured particle flux at 1 AU to the corresponding value the location of our test planet (0.153 AU). For this, we assume steady-state conditions, allowing us to use the scaling for the total event fluence for the instantaneous particle flux, leading to

$$\text{flux}(d) = \text{flux}(1\text{AU}) * \left(\frac{d}{1\text{AU}}\right)^\beta \quad (1)$$

We use an energy-independent value of $\beta = -2.0$ (see discussion in Grenfell et al. 2012 for details). The resulting cosmic ray energy spectra reaching the top-of-atmosphere of our test planet are shown in Fig. 1. The SCR spectra show strongly increased fluxes at lower energies and lower fluxes at higher energies compared to the GCR case for Earth. The CR flux is input into the atmosphere model to simulate different stellar activities and hence cosmic radiation environments on the modelled planet, which influence planetary climate and photochemistry.

As our model converges to steady-state, the proton fluxes for these scenarios are assumed to be constant. With this in mind, the flaring M-dwarf case described in scenario 4 requires further explanation. Grenfell et al. (2012) assume that the frequency of flares for strongly flaring M-dwarfs is fast when compared with the chemical relaxation time scales in the middle atmosphere of Earth-like planets. That said, a constantly flaring M-dwarf shows in itself flares of highly irregular intensity. We take the flaring scenario as an upper limit although more observations of flaring M-dwarfs are needed.

2.2. Atmosphere model

The one-dimensional, radiative-convective atmosphere model and the photochemical model used in this work were originally developed to simulate atmospheric scenarios of the early Earth (see Kasting et al. 1984, 1985). Both models were first coupled by Segura et al. (2003) to study the effect of different stellar spectra on the detectability of biosignatures on their host star.

We use the new version of this model, described in Grenfell et al. (2012); Rauer et al. (2011) and references therein, to simulate an Earth-like (i.e. N_2 , O_2 dominated) atmosphere. For the Earth-like scenarios considered here we focus on responses from the troposphere up to the middle atmosphere (typically at 60-70km) since this region is expected to be important for biosignatures such as ozone and nitrous oxide. The two coupled submodules are described in the following.

2.2.1. Climate module

The climate module calculates globally, diurnally averaged temperature, pressure and water profiles by assuming two energy transport mechanisms: radiation and convection. The model ranges from the surface to a pressure level of $6.6 \cdot 10^{-5}$ bar using a variable pressure grid. As initial values, the bulk composition, temperature, and pressure are set to modern Earth profiles based on the U.S. Standard Atmosphere (COESA, 1976). The surface albedo is fixed to 0.2067 and the gravitational acceleration to 9.8 m/s^2 . The radiative transfer scheme for the incoming stellar short-wave spectrum (ranging from 237.6 nm to $4.545 \mu\text{m}$) is calculated using the δ -two-stream method (Toon et al. 1989). The scheme incorporates visible and near-IR absorption by O_2 , O_3 , CH_4 , and CO_2 and H_2O as well as Rayleigh scattering for N_2 , O_2 , and CO_2 . The long-wave (3.33 – $1000 \mu\text{m}$) transfer is handled by the Rapid Radiative Transfer Model (RRTM; Mlawer et al. 1997), which takes continuum and gaseous opacity of H_2O , CO_2 , CH_4 , O_3 , N_2O into account. Both long and short-wave schemes use the correlated-k method. In the IR, the k-coefficients are precalculated for a specific range in composition, temperature, and pressure, the validity range of the model ranges from 0.01 to 1050 mbar and within $\pm 30 \text{ K}$ of the global-mean Earth temperature profile. Below the tropopause the temperature profile is determined by a wet adiabatic lapse rate, based on Kasting (1988) and Ingersoll (1969), using the relative humidity profile of Manabe & Wetherald (1967).

The climate module converges when the relative temperature difference between two adjacent iteration steps does not exceed a value of 10^{-7} in all levels and the total radiative flux (downwards and upwards) at top of atmosphere is less than 10^{-3} W/m^2 for a timestep larger than 10^4 seconds. The module then outputs converged to steady-state solutions for the globally and diurnally-averaged temperature, pressure, and water profiles, which are then passed on to the chemistry module.

2.2.2. Chemistry module

The chemistry module calculates the steady-state solution of a photochemical network of over 200 reactions of 55 species, which are important for biomarker and greenhouse gas chemistry on a planet with an Earth-like development. The scheme thereby solves a set of non-linear continuity equations using an implicit Euler method. When the species' concentrations converge, loss rates (e.g. due to gas-phase in-situ sinks, condensation, deposition at the lower boundary, wet deposition, etc.) are then in balance with species' production rates (e.g. due to gas-phase in-situ sources, evaporation, emission and effusion fluxes at the model boundaries, etc.).

We assume modern Earth values for well-mixed isoprofile species ($N_2 \approx 0.78$, $O_2 = 0.21$, $Ar = 0.01$ and $CO_2 = 3.55 \cdot 10^{-4}$ volume mixing ratio) and for surface biogenic fluxes of for example CH_3Cl , N_2O , and CH_4 (see Grenfell et al. 2013). An eddy diffusion coefficient profile (Massie & Hunten 1981) is used to

parameterise the vertical transport of species between model layers. The chemical scheme includes photolysis rates for the major absorbers and more than 200 chemical reactions including the essential chemical families Ox, HOx, NOx, and SOx, and is designed to reproduce the ozone profile on modern Earth. More details of the chemical network scheme are provided in Kasting et al. (1985), Segura et al. (2003) with recent updates described in Rauer et al. (2011).² The reaction rates are set to the recommendations of the JPL 2003 report (Sander et al. 2003). Photolysis rates in the chemistry module are calculated for ten far-UV wavelength intervals from 120-175 nm, i.e. including Ly-alpha, which is important to capture water photolysis in the upper atmospheric layers for example. The remaining 108 wavelength intervals range from 175.4 -855.0 nm. The intensity of the photon flux is calculated with the δ -two stream method (Toon et al. 1989) for 175.4 -855.0 nm and with Beer-Lambert's law for 120-175 nm.

The chemistry module converges when all species concentrations in all model layers change by less than 10^{-4} of their relative amount between adjacent iteration steps with $dt > 10^5$ seconds. The resulting converged profiles of the radiative species are passed back to the climate module. This process iterates until the whole model converges to a steady-state solution, which is reached when the relative difference of the temperature profiles of two consecutive radiative-convective/photochemical iterations does not exceed 10^{-5} . This is satisfied in most cases after 70-100 iterations.

2.3. Improvements to the cosmic ray scheme

The original model described in Grenfell et al. (2007a, 2012) uses an atmospheric air-shower approach to simulate CR-induced NO production rates (which were fed into the chemistry module) from incident primary particles at TOA. The only primary particles taken into account are protons, which in turn produce only secondary electrons. Particles are assumed to propagate in straight lines, according to their initial incident angle. This approach is usually valid for particle energies between TeV and EeV (Alvarez-Muniz et al. 2002). In our model, however, we apply this approach for particle energies of MeV - TeV. Thereby we make use of extrapolated values for the Gaisser-Hillas-Function (see Sect. 2.3.3). The resulting secondary electron fluxes reproduce the measured maximum of ionizing radiation by CRs at $15 \pm 2 \text{ km}$, also called the "Pfozter maximum" (Pfozter 1936).

In the current work, we utilise an improved version of the cosmic ray scheme used by Grenfell et al. (2012). The key updates include

- an improved CR-induced production of NOx molecules and a new CR-induced HOx production based on the ion-pair production rate (IPR) from CR particles (Sect. 2.3.1)
- an improved, energy-dependent impact cross-section of CR-induced secondary electrons (Sect. 2.3.2)
- updates to the parameters of the Gaisser-Hillas scheme used by Grenfell et al. (2012) (Sect. 2.3.3)

² Further detail on the species, absorption coefficients, chemical reaction network, etc. can be found in the following link <http://vpl.astro.washington.edu/sci/AntiModels/models09.html> for a version of the model code as described by Segura et al. (2003, 2005).

2.3.1. NO_x and HO_x production via ion pair production rate

The CR scheme used in this work uses an air-shower approach based on the parametrisation by (Gaisser & Hillas 1977) to derive secondary electron fluxes. In previous works (e.g. Grenfell et al. 2007a, 2012), it was assumed that these electrons directly produce NO via



with the assumption that $k_{\text{NO}_x} = 1$, i.e. one NO molecule would be produced on average per destroyed N₂ molecule. Thus Grenfell et al. (2007a, 2012) use an ion pair production parametrisation with a production rate of 1 NO per ion pair (Nicolet 1975).

The current work improves upon this scheme by parametrically taking into account ionic products of the CR-induced destruction of the main atmospheric constituents N₂ and O₂, adding a HO_x production parametrisation, as well as incorporating branching ratios of the produced NO_x and HO_x species. This approach is necessary when modelling HO_x production as one would otherwise have to incorporate a complex ion chemistry network involving ionic water clusters (see e.g. Verronen & Lehmann 2013).

We compute the IPR (ion pair production rate) by summing up the ionisation rates by electron impact for N₂ and O₂, i.e.

$$\text{IPR}(X) = \sum_{i=\text{N}_2, \text{O}_2} \int_{E_1}^{E_2} n_i(X) \cdot \sigma_{\text{ion}(i)}(E_{el}) \cdot F_{el}(X, E_{el}) dE_{el} \quad (4)$$

where $\text{IPR}(X)$ is the ion pair production rate for the layer with mass column density X , n_i is the number density of species i , $\sigma_{\text{ion}(i)}$ is the total ionisation cross-section of chemical species i by electron impact, and F_{el} the flux of secondary electrons. The integral over electron energy E_{el} is confined by the energy range (E_1, E_2) of $\sigma_{\text{ion}(i)}$, i.e. ~ 10 to 1000 eV for the current work. The ionisation cross-sections for N₂ and O₂ are given in Fig. 2.

For this approach, production coefficients k are used not only for NO_x production where $k_{\text{NO}_x} = 1.25$ (Porter et al. 1976; Jackman et al. 1980), but also for the production of HO_x where $k_{\text{HO}_x} = 2$ (Solomon et al. 1981).

A further improvement is that we take into account branching ratios for both NO_x as well as HO_x species, which are well known. The reaction of N₂ with CRs results in 45% of ground state nitrogen N(⁴S) and 55% excited state nitrogen, e.g. N(²D), N(²P) (Jackman et al. 2005; Porter et al. 1976). In accordance with Jackman et al. (2005), we do not directly include N(²D) in our chemical scheme, but assume that the reaction



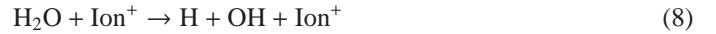
proceeds instantly while ground state N can either produce or destroy NO via



depending on the pressure and temperature of the surrounding medium.

The parameter k_{HO_x} strongly depends on the amount of available atmospheric H₂O. For the purposes of the current work, we assume the maximum value $k_{\text{HO}_x} = 2$ as we are interested in altitude regions below 60 km (compare with Fig. 2 in Solomon et al.

(1981)) and our model atmospheres provide sufficient H₂O concentrations in that region. For HO_x a production coefficient k_{HO_x} of 2 HO_x molecules per ion pair produced is equivalent to the destruction of a water molecule (with $k_{\text{H}} = k_{\text{OH}} = 1$):



Recent studies by Sinnhuber et al. (2012) have found that $k_{\text{OH}} = 0.9$ in the mesosphere, yet testing this change (not shown) had little to no effect on our results.

2.3.2. Energy dependent electron-impact cross-sections

The above mentioned additions to our rather simple air-shower scheme provide a motivation to improve our model input parameters in the CR scheme. The electron impact cross-section σ is one such parameter. Our previous studies (Grenfell et al. 2007a, 2012) have used a constant value for the electron impact cross-section for N₂ of $\sigma_{\text{N}_2} = 1.75 \cdot 10^{-16} \text{ cm}^2$ (Nicolet 1975) for electron energies between 30eV and 300eV (and $\sigma_{\text{O}_2} = 0$). The current work uses energy dependent total ionisation cross-sections $\sigma_{\text{ion}(\text{N}_2)}$, $\sigma_{\text{ion}(\text{O}_2)}$, which are needed to calculate the ion pair production rate via Eq. 4.

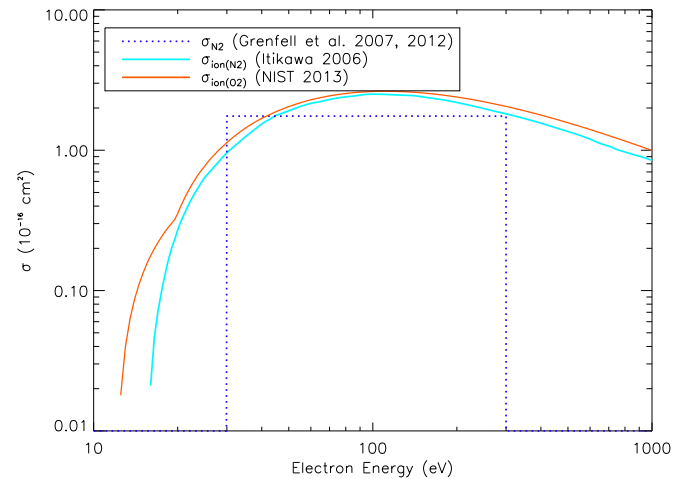


Fig. 2. Comparison of previously used cross-section $\sigma_{\text{N}_2} = 1.75 \cdot 10^{-16} \text{ cm}^2$ and new total ionisation cross-sections $\sigma_{\text{ion}(\text{N}_2)}$ (Itikawa 2006) and $\sigma_{\text{ion}(\text{O}_2)}$ (NIST 2013).

Figure 2 shows both the old, constant value of σ_{N_2} as well as our updated N₂ and O₂ ionisation cross-sections. Using the new values better reflects the contribution of the involved particles according to their energies. The overall impact of these and all further changes is shown in Sect. 2.3.4.

2.3.3. Expanding energy range and improving energy dependence of the input parameters of the Gaisser-Hillas scheme

Since Griebmeier et al. (2015b) work with primary protons with an extended energy range of 16 MeV to 0.5 TeV (compared to the previously-used range of 64 MeV to 8 GeV), the parameters of the Gaisser-Hillas formula need to be extended as well. The scheme is detailed by Grenfell et al. (2007a), but we nevertheless give a short review here.

We wish to calculate the secondary electron flux F_{el} from the top-of-atmosphere proton flux, so that F_{el} can then be input into

E_p [MeV]	64	128	256	512	1024	2048	4096	8192
X_0 [g/cm ²]	0.001	1	2	80	80	80	80	80
X_{max} [g/cm ²]	0.01	5	25	150	150	150	150	150
N_{max}	3	3	3	3	3	3	3	3

Table 1. Parameters of the Gaisser-Hillas function (Eq. 13) following Grenfell et al. (2012)

Eq. (4). At first F_{el} is separated into

$$F_{el}(X, E_e) = R_{el}(X) \cdot S_{el}(E_e), \quad (9)$$

the total electron flux R_{el} and the spectral distribution of electrons $S_{el}(E_e)$, which is assumed to follow a power law (Grenfell et al. 2007a)

$$S_{el}(E_e) = a \cdot E_e^{-3} \quad (10)$$

with the criterion that $S_{el}(E_e)$ is normalised over the whole energy range

$$\int S_{el}(E_e) dE_e = 1. \quad (11)$$

As we see during the validation in Sect. 2.3.4, measurements of the resulting NO production rate are best reproduced when the parameter a in Eq. (10) is set to a value of 18 eV².

The total electron flux R_{el} from equation (9) is obtained by

$$R_{el}(X) = \int_{\Omega} d\Omega \int_{E_p} N_{el,p}(X, \theta, \phi, E_p) \cdot F_p(X=0, E_p) dE_p, \quad (12)$$

where Ω is the solid angle and $N_{el,p}$ is the number of electrons produced by one primary proton with energy E_p and an incident direction (θ, ϕ) (Grenfell et al. 2007a).

We obtain $N_{el,p}$ using the Gaisser-Hillas formula

$$N_{el,p}(X', E_p) = N_{max}(E_p) \cdot e^{\frac{X_{max}(E_p) - X'}{\lambda(E_p)}} \cdot \left(\frac{X' - X_0(E_p)}{X_{max}(E_p) - X_0(E_p)} \right)^{\frac{X_{max}(E_p) - X_0(E_p)}{\lambda(E_p)}}, \quad (13)$$

which was as first introduced as a fit function for high-energy cosmic ray measurements (Gaisser & Hillas 1977). The equation yields the number of secondary electrons produced $N_{el,p}$, dependent on the mass column density X' in the trajectory of the primary particle and its energy E_p . The column density along a trajectory X' at a given height z depends on the incident angle θ of the proton and the mass column density at z ,

$$X'(z) = \frac{X(z)}{\cos(\theta)}. \quad (14)$$

The free parameters of Eq. (13) are the position X_{max} of the electron maximum, the number N_{max} of secondary electrons at X_{max} , the proton attenuation length X_0 , and the electron attenuation length $\lambda = 40$, where X_{max} , X_0 , and λ are each in units of mass column density, i.e. g/cm². Table 1 lists the parameters used by Grenfell et al. (2012). We now address each of these parameters in turn.

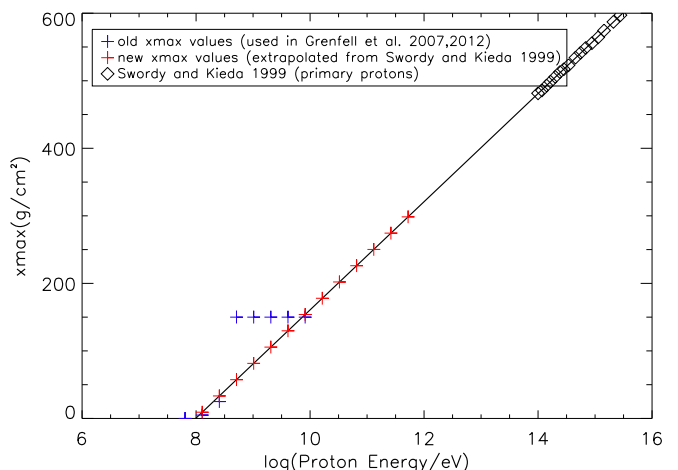


Fig. 3. Values for X_{max} from Swordy & Kieda (2000) (black diamonds). We extrapolated the values to 64 MeV - 0.5 TeV (red crosses) for the current study. Also shown are the values for X_{max} as used by Grenfell et al. (2012) (blue crosses).

Proton attenuation length X_0 : For this parameter we adopt the air-shower approach of Alvarez-Muniz et al. (2002), who also use the Gaisser-Hillas function, but assume $X_0 = 5$ g/cm² as the depth of the first interaction. We therefore set X_0 to 5 g/cm² for proton energies equal to 512 MeV and above. This has the effect that the peak of our resulting secondary electron flux, previously situated rather sharply at an altitude of about 15 km for Earth, spreads over a wider region, thereby corresponding better to Earth measurements (see Sect. 2.3.4 and Fig. 4).

For energies below 512 MeV, the air-shower scheme applied here loses accuracy as it is better applied to high-energy primary particles. This outcome is most easily seen, when $X_0 > X_{max}$, as this would produce negative fluxes in Eq. (13). Furthermore, primary protons of such low energy are normally not involved in particle cascades or air-showers, but rather lose energy directly to the atmosphere via ionisation (Usoskin et al. 2009). To address this problem, we lower the values of X_0 for primary protons with energies below 512 MeV to the values shown in Table 2 and 3. This means these protons interact with the atmosphere at higher altitudes in our model, which acts as an approximation of their energy loss via ionisation of the upper atmosphere.

Position of the electron maximum X_{max} : This parameter is strongly energy dependent, so it needs to be addressed accordingly when expanding the energy range. In their Fig. 1, Swordy & Kieda (2000) give theoretical values of X_{max} for incident protons from 100 TeV to 10 PeV.

Figure 3 shows an extrapolation of the values obtained from Swordy & Kieda (2000) to the energy range relevant to this work. The extrapolated values take the expected energy dependence of X_{max} into account and show reasonable agreement with the previously used values at 100 MeV and 10 GeV.

In the previous CR scheme, the effect of CR protons with energies lower than 64 MeV were not included. These may, however, play an important role for the simulation of the effect of SCRs upon the atmosphere, as SCR proton spectra feature many primary protons with energies lower than 64 MeV (Wissing & Kallenrode 2009) (see also Fig. 1). As suggested above, the range of validity of our model reaches its limit at low energies. Nevertheless, a rough assumption is made here for energies between 16 - 64 MeV. Monte-Carlo simulations

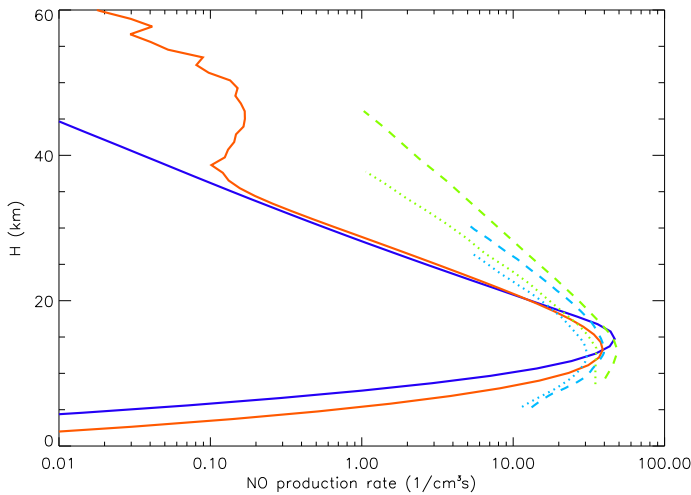


Fig. 4. Comparison of GCR-induced NO production rates, showing model output for the original scheme (Grenfell et al. 2012, dark blue solid curve) and the new scheme (red solid curve) as well as Earth measurements from Nicolet (1975) for solar maximum (blue dotted curve) and solar minimum (blue dashed curve) and from Jackman et al. (1980) for solar maximum (green dotted curve) and solar minimum (green dashed curve).

of downwards proton transfer in the atmosphere performed by Wissing & Kallenrode (2009) (their Fig. 2) suggest values for X_{max} in the stated energy range, which are given in Table 2. We assume the proton attenuation length X_0 to scale accordingly.

E [MeV]	16	32	64
X_{max}	0.01	0.65	1.7
X_0	0.001	0.01	0.1

Table 2. Parameters for lower energy ranges, adapted from Wissing & Kallenrode (2009).

Maximum number of electrons N_{max} : The maximum number of electrons produced per proton (at X_{max}) is also highly energy dependent, but was used as a freely-adjustable factor in previous works. Alvarez-Muniz et al. (2002) provide an analytical relation, with a validity range of $10^{14} - 10^{19}$ eV

$$N_{max} = 0.75 \cdot \frac{E_p}{\text{GeV}} \quad (15)$$

As with the previous parameters, we also extrapolate this relation to the energy range relevant for this work (see Table 3).

2.3.4. Model validation

The different model components have been validated as follows: **GAS-PHASE CHEMISTRY** - Grenfell et al. (2013) showed that the model (without CRs) calculates a (global, annual mean) ozone column of 305 Dobson Units is in agreement with modern Earth observations. That work also showed that the Chapman mechanism producing ozone dominates in the model stratosphere, peaking near the observed ozone maximum, and that the so-called smog mechanism dominates in the troposphere. These findings are in-line with current understanding of ozone photochemistry on the modern Earth. That work also presented column values for other (in addition to ozone) biosignature can-

didates, related source gases as well as surface UV which suggested that the model reproduces the modern Earth reasonably well. Grenfell et al. (2011) found reasonable agreement between the surface biomass fluxes required in the chemistry module to reproduce the modern Earth atmospheric composition and the observed values for these fluxes.

RADIATIVE TRANSFER - Rauer et al. (2011) showed temperature profiles for the modern Earth which suggested that the model reproduces observations of the modern Earth reasonably well.

THIS WORK, COSMIC RAY SCHEME - SCRs are difficult to validate with Earth observation using our stationary (i.e. without time dependence) model because they are a time-dependent phenomenon so we here focus only on GCRs. There are three points to consider:

Firstly, the effects of secondary electrons produced from air-shower schemes are commonly validated by comparing the computed ion pair production rates (IPR) with those observed. Our model-calculated IPR (which is the NO production of Fig. 4 rate divided by $k_{NOx} = 1.25$, see Sect. 2.3.1) falls within the range calculated by Velinov & Mateev (2008) between solar minimum and maximum in the middle stratosphere i.e. 3 to 30 ion pairs per $\text{cm}^{-3} \text{s}^{-1}$, depending on solar cycle phase and altitude.

Secondly, the high-energy secondary electrons break up the strongly-bound N_2 molecule, and the resulting nitrogen atoms quickly react with oxygen-containing species which leads overall to an enhanced production rate of NO (see Fig. 4). We compare our modelled production rate of nitrous oxide (NO) with data derived from measurements by Nicolet (1975) and Jackman et al. (1980). Using the improvements described in Sect. 2.3.3, we calculate the NO production rate as shown in Fig. 4. The blue solid curve used the original scheme, while the solid red curve used the improvements presented in sections 2.3.1 – 2.3.3. The remaining curves show data obtained from measurements by Nicolet (1975) and Jackman et al. (1980), respectively, for minimum and maximum solar activity at 60° geomagnetic latitude. We see an improvement when comparing the NO production rates of both the current and previous work. Overall the new scheme produces a broader peak below 20 km, which is shifted down in altitude and whose maximum is slightly reduced, thereby producing better agreement with the measured rates. This effect is especially evident at altitudes below 13 km, which are due to the incorporation of higher energy incident protons. These higher energy protons affect lower altitudes due to increasing X_{max} values with proton energy (see Sect. 2.3.3). Additionally, high-energy protons have a greater effect on the atmosphere due to higher values of N_{max} for higher energies. The peak NO production for the new scheme is broadened because of the change in X_0 . The parameter a (see Eq. 10) was set to 18 eV^2 to move the peak value into the range of measured NO production rates. Above 35 km the effects of the new IPR scheme (see Sect. 2.3.1) are particularly evident. In this region the branching between NO-producing and NO-destroying effects of ground-state nitrogen (see Eqs. 6 + 7) favours NO production. The curve is slightly jagged because of the non-linear dependence of Eqs. (6) and (7) upon pressure, temperature and concentration. In the altitude region between 20 and 35 km the model results underestimate the observations. While adding a background SCR spectrum to the incident protons could mitigate this discrepancy to some extent, the most probable cause is that we need to better address the gradual loss of proton energy via ionisation of the atmosphere. This issue is beyond the scope of the current work. Nevertheless, we are able to reproduce the effects of the Pfozter maximum using both old and new

E [MeV]	16	32	64	128	256	512	1024	2048
X_0	0.001	0.01	0.1	1	2	5	5	5
X_{max}	0.01	0.65	1.7	9.2	33.3	57.4	81.5	105.6
N_{max}	0.125	0.25	0.05	0.10	0.19	0.38	0.77	1.54

E [MeV]	4096	8192	16384	32768	65536	131072	262144	524288
X_0	5	5	5	5	5	5	5	5
X_{max}	129.7	153.8	178.0	202.0	226.2	250.3	274.4	298.5
N_{max}	3.07	6.14	12.29	24.58	49.15	98.30	196.61	393.22

Table 3. Updated set of Gaisser-Hillas parameters with improved energy dependence and expanded energy range.

schemes, and both modelled curves show good agreement to the data obtained from measurements in this region. However, the new scheme works with ionic secondary particles so that NOx and HOx production parametrizations can be calculated via the IPR approach. In addition the energy ranges for primary particles were extended from 64 MeV - 8192 MeV to 16 MeV - 524288 MeV and our new scheme uses updated input parameters that are energy dependent, which allows for primary particles to produce a different number of secondaries depending on their initial energy.

Thirdly, the model calculates a concentration of NO based on its sources and sinks (including the GCR source). The modern Earth scenario (including GCRs) produces a concentration of nitrogen monoxide (NO) of 12 ppbv at 40 km which is consistent with modern Earth observations (see e.g. Sen et al. 1998). However, this species varies both diurnally and over latitude so a clear consensus of its global average (i.e. as calculated in our model) is not available.

While it would be desirable to validate directly with OH production, OH is a difficult species to observe especially in the stratosphere. OH is a highly reactive trace species and its stratospheric mean value is not well known. Faced with the lacking observations, some recent 3D model studies from the Earth science community have been recently applied to estimate the effect of GCRs on HOx. For example, Calisto et al. (2011) reported HOx decreases due to GCRs of 1-3% in the stratosphere. Our model calculates a column response of 3% decrease of HOx (H + OH + HO₂) due to CRs. While these values are broadly comparable they cannot be directly compared to the 3D model study of Calisto et al. (2011) as that study does not provide global mean values. In a similar fashion the response of O₃ concentrations can be mentioned. Our model calculates an integrated column density loss of O₃ of less than 1% due to GCRs on Earth, while Calisto et al. (2011) find that GCR cause up to 3% loss of O₃ in the polar stratosphere and upper troposphere as well as an increase in O₃ of up to 3% in the tropics and south polar troposphere.

2.4. Line-by-line spectral model

We use a radiative transfer line-by-line tool called SQuIRRL (Schwarzschild Quadrature InfraRed Radiation Line-by-line) (Schreier & Schimpf 2001; Schreier & Böttger 2003). This tool uses a radiative transfer method with line-by-line absorption from the HITRAN 2004 database (Rothman et al. 2005) to compute planetary spectra of H₂O, CO₂, O₃, CH₄, N₂O, CO, SO₂, NO₂, NO, HCl, HNO₃, H₂O₂, HO₂, CH₃Cl, OH, ClO, and ClONO₂. The converged density profiles of the above mentioned species, as well as pressure and temperature from the atmospheric column model are input into SQuIRRL.

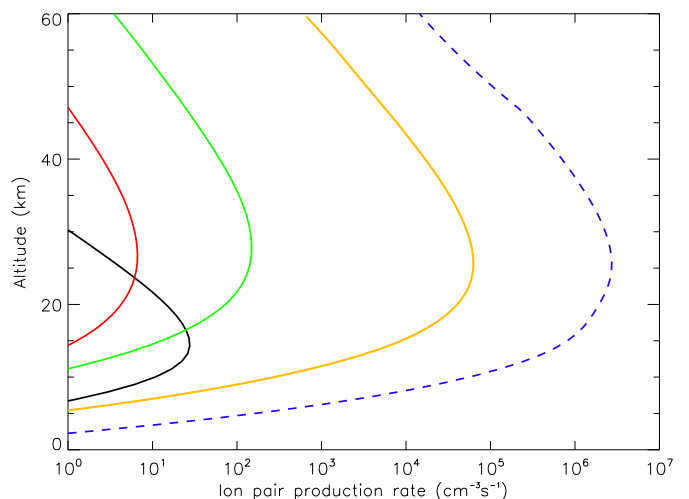


Fig. 5. Ion pair production rates as output by the CR air-shower scheme. Shown are: scenario 0 (GCR Earth, black curve), scenario 2 (quiescent M-dwarf, red curve), scenario 3 (active M-dwarf, green curve), scenario 4 (flaring M-dwarf, yellow curve), as well as the flaring case from Grenfell et al. (2012) (dashed blue curve, scenario 6).

3. Results

3.1. Atmospheric profiles

3.1.1. Ion pair production rates

Figure 5 shows the model output ion pair production rates (see Eq. 4) for the incident proton spectra shown in Fig. 1. Solid lines were calculated using the new scheme, while the dashed line originates from the scheme as used by Grenfell et al. (2012). The modelled IPR of GCRs (black line) and SCRs (coloured lines) in Fig. 5 peak at decidedly different altitudes, with GCRs peaking at around 14 km and SCRs at 25 to 30 km altitude. While the IPR is relatively small for the quiescent M-dwarf case (red line), the IPR intensity increases significantly with activity of the host star (green and yellow lines).

Noteworthy is the change in IPR intensity when comparing the flaring M-dwarf scenario of this work with that of Grenfell et al. (2012). The new scheme results in an IPR at its maximum that is roughly 40 times smaller than the IPR produced by Grenfell et al. (2012). This significant change in the effect of CRs is a direct result of our updated input parameters (see Sect. 2.3.3). In particular, the expansion of the energy range of the Earth GCR validation run with energies > 8.2 GeV, together with $N_{max}(E) \sim E$, significantly increases the contribution of CR particles with $E > 8.2$ GeV to the validation spectrum. The SCR fluxes of these high energies are, however, negligibly small when compared to the maximal SCR flux. Hence the

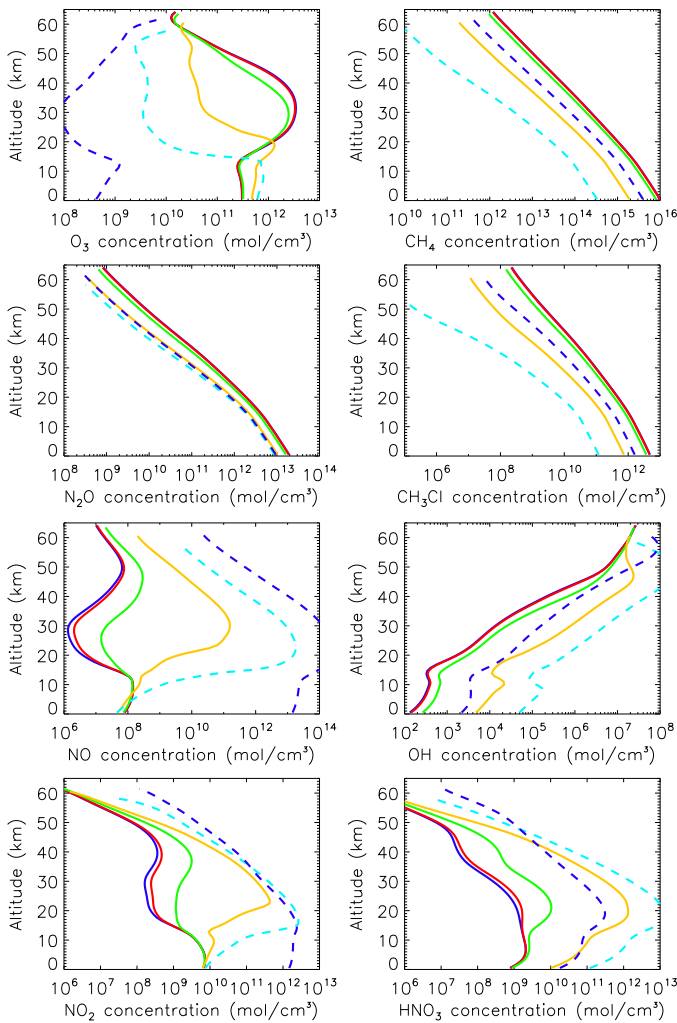


Fig. 6. Chemical concentration profiles for biomarker species O_3 , CH_4 , N_2O , and CH_3Cl and for related species NO , OH , NO_2 , and HNO_3 in molecules per cm^3 . Shown here are scenarios 1 through 5: M-dwarf w/o CR (solid dark blue line), quiescent M-dwarf (red line), active M-dwarf (green line), flaring M-dwarf (yellow line), flaring(x40) M-dwarf (light blue dashed line). In addition we show the result of Grenfell et al. (2012)’s flaring case (dark blue dashed line) for comparison.

overall SCR-induced IPR profiles decrease because the influence of $E > 8.2$ GeV GCR protons is increased. While the updated scheme provides a more physically valid parametrisation of the effect of cosmic ray ionisation (especially regarding the energy dependence of the parameters), we nevertheless wish to compare the chemical effects of our improved scheme with those of the original. For this purpose we include two new scenarios in our analysis as shown below:

5. **flaring(x40) M-dwarf**: same as scenario 4, but with 40 times enhanced IPR.
6. **flaring M-dwarf (Grenfell et al. 2012)**: same as scenario 4, but with the original version of the CR scheme as described by Grenfell et al. (2012).

3.1.2. Chemistry profiles

Figure 6 shows chemical profiles for the biomarker species O_3 , CH_4 , N_2O , and CH_3Cl as well as the related species NO , OH , NO_2 and HNO_3 for scenarios 1 through 6. The M-dwarf w/o

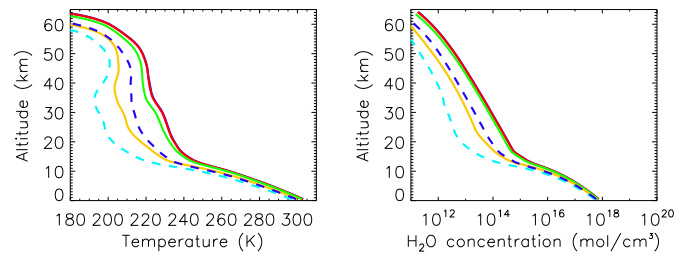


Fig. 7. Temperature and H_2O concentration profiles for scenarios 1-6. Colouring scheme same as above.

CR (blue line) is very similar to the AD Leo case of Rauer et al. (2011), as we use the same version of the atmospheric model. Increasing the CR intensity has noticeable effects on the modelled atmospheres. While only small changes in the NO , NO_2 and HNO_3 concentrations are observed for the quiescent M-dwarf, the active and flaring scenarios (scenarios 3 and 4) show significant variations. The active case shows a column-integrated decrease in O_3 by 30% and CH_4 by 15% as well as a 300% increase in HNO_3 compared to scenario 1 (w/o CR). The flaring scenario (4) shows a column-integrated O_3 decrease by over 70% and CH_4 by 80% and a significant increase of HNO_3 by a factor of 315. A detailed list of column-integrated concentrations of key species can be found in Table 4. In general CRs lead to the photochemical destruction of O_3 , CH_4 , N_2O , and CH_3Cl . Because of the large amount of CR-induced NO_x and HO_x , these species are increasingly stored as HNO_3 with increasing CR intensity.

When comparing scenarios 5 and 6, the effects of the newly introduced CR-induced NO_x and HO_x production is clearly evident (as both scenarios calculate a similar IPR). Scenario 6 calculates a reduction in O_3 by 99.99% because of the excessive amount of NO produced which destroys O_3 catalytically in the middle atmosphere. In scenario 5 this effect is mitigated by the additionally produced OH , which converts NO_x into HNO_3 , mainly via



Without CRs (case 1) the modelling of Earth-like planets orbiting in the HZ of M-dwarfs results in up to 300 times as much CH_4 compared to the reference case (see also Segura et al. 2005; Rauer et al. 2011). This so-called massive CH_4 greenhouse effect can strongly perturb climate and habitability. However, when adding CRs including the updated HO_x -production scheme (cases 2,3,4,5), this CH_4 is more efficiently destroyed, as the produced OH acts as a strong CH_4 sink via



so that for the flaring M-dwarf (case 4) only 50 times as much CH_4 is available compared to the Earth reference case. A similar mechanism is responsible for the large decrease in CH_3Cl . N_2O concentrations, on the other hand, are not greatly influenced by the changes to the scheme. Overall, this shows that the CR-induced HO_x chemistry and the nitrogen radical production introduced to this work has an important effect and may not be neglected in scenarios with strong SCR flux.

3.1.3. Temperature and water profiles

The planetary temperature profile for the scenarios with the M-dwarf spectrum we used usually shows no stratospheric temperature inversion, since the stellar UV flux is too weak to warm

# Scenario	O ₃ [DU]	CH ₄ [DU]	N ₂ O [DU]	CH ₃ Cl [DU]
0 Earth reference	306	1.2·10 ³	233	0.35
1 M-dwarf w/o CR	254	3.3·10 ⁵	630	160
2 quiescent M-dwarf	243	3.2·10 ⁵	620	150
3 active M-dwarf	175	2.7·10 ⁵	530	120
4 flaring M-dwarf	71	6.5·10 ⁴	350	24
5 flaring(x40) M-dwarf	40	1.1·10 ⁴	300	4
6 flaring M-dwarf (Grenfell et al. 2012)	0.2	1.3·10 ⁵	310	53

# Scenario	NO [DU]	OH [DU]	NO ₂ [DU]	HNO ₃ [DU]
0 Earth reference	1.4·10 ⁻¹	2.1·10 ⁻³	0.2	0.6
1 M-dwarf w/o CR	9.8·10 ⁻³	8.4·10 ⁻⁴	0.3	0.2
2 quiescent M-dwarf	1.0·10 ⁻²	8.4·10 ⁻⁴	0.3	0.2
3 active M-dwarf	2.3·10 ⁻²	8.9·10 ⁻⁴	0.5	0.6
4 flaring M-dwarf	7.3·10 ⁰	1.5·10 ⁻³	16	63
5 flaring(x40) M-dwarf	8.7·10 ²	1.0·10 ⁻²	100	600
6 flaring M-dwarf (Grenfell et al. 2012)	1.6·10 ⁴	3.1·10 ⁻³	170	16

Table 4. Column densities of O₃, CH₄, N₂O, CH₃Cl, NO, OH, NO₂, and HNO₃ in Dobson units (1DU = 2.69 · 10²⁰ molecules/m²) for scenarios 0 through 6.

the stratosphere. Figure 7 shows that with increasing cosmic radiation the temperature in this region generally cools by up to 30 K owing to the loss of key radiative gases (e.g. CH₄, O₃). Since CH₄ abundances are significantly higher than on Earth (by factors between 10 for scenario 5 and 300 for scenario 1; see Table 4) there is a potentially significant methane greenhouse as pointed out in previous works (see e.g. Segura et al. 2005; Grenfell et al. 2007a).

The effect on temperature of using the new NO_x and HO_x production scheme is evident from comparing the flaring scenarios 4 (yellow curve) and 6 (dark blue dashed curve): between 10 and 50 km altitude temperature curves of scenarios using the new scheme are markedly lower. This decrease in temperature follows from decreased CH₄ concentrations (see Sect. 3.1.2 and Fig. 6). H₂O concentrations relate well with CH₄, which is expected as they are highly interdependent via Eq. (17).

3.2. Identifying significant chemical mechanisms

To further identify important chemical mechanisms caused by the update of our CR scheme we have repeated runs of the flaring M-dwarf scenario (scenario 4), but this time with different CR-induced production mechanisms turned on. We investigate the following cases:

- 4.0. **flaring M-dwarf (NO_x+HO_x):** same as 4, hence producing CR-induced NO, N, OH, and H.
- 4.1. **flaring M-dwarf (NO_x):** same as 4, but only produces NO and N due to CR.
- 4.2. **flaring M-dwarf (HO_x):** same as 4, but only produces H and OH due to CR.
- 4.3. **flaring M-dwarf (NO):** same as 4, but only produces NO due to CR, i.e. as in Grenfell et al. (2012) and otherwise using the updated Gaiser-Hillas scheme (see Eq. 13).

Figure 8 shows the effects of different CR-induced production mechanisms. When comparing scenarios 4.3 and 4.1, one can infer that the O₃ destroying species NO is hampered in its catalytic destructivity in scenario 4.1 by CR-produced atomic N radicals, as significantly more O₃ is observable here. This is caused by a self-regulating mechanism imposed by the CR-induced production of nitrogen radicals (N(⁴S)), as these can easily reconfigure

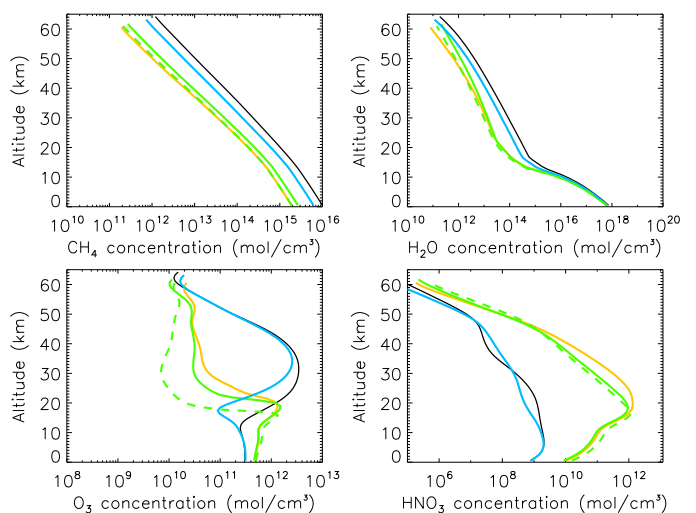


Fig. 8. Chemical concentration profiles for species CH₄, H₂O, O₃ and HNO₃ in molecules per cm³ for scenarios 4.0 - 4.3 (see Sect. 3.2) with the following CR-induced production mechanisms switched on: NO_x+HO_x (scenario 4.0, solid yellow curve), NO_x (scenario 4.1, solid green curve), HO_x (scenario 4.2, solid blue curve), NO (scenario 4.3, dashed green curve). Scenario 1 (M-dwarf w/o CR) is shown for comparison (solid black curve).

into N₂, via e.g.



Another interesting mechanism is evident when comparing the O₃ concentrations for scenarios 4.0, 4.1, and 4.2. Both the HO_x (scenario 4.2) as well as the NO_x (scenario 4.1) producing schemes, lead to a decrease in O₃, in each case via catalytic destruction with HO_x and NO_x species, respectively. The NO_x scheme destroys O₃ most effectively from 20 to 60 km altitude (see green solid curve in Fig. 8, bottom left), while the HO_x scheme is most effective from 10 to 40 km (see solid light solid blue curve in Fig. 8, bottom left). The catalytic NO_x-cycle significantly outweighs the HO_x cycle. While both separately remove O₃, when combined (4.0, solid yellow line, Fig. 8), HO_x and NO_x production schemes cause an increased O₃ profile com-

pared with the dominant NO_x cycle of scenario 4.1. This increase in O₃ arises from the storage of both NO_x and HO_x O₃-destroying species in the unreactive reservoir species HNO₃, formed mainly via



Contrary to the O₃ destruction result, NO_x and HO_x production schemes reinforce each other with respect to destroying CH₄. This is likely due to both schemes producing OH, either via direct H₂O destruction (HO_x scheme), through the NO_x scheme via, e.g.



which is ten times faster for scenario 4 compared to Grenfell et al. (2012) (scenario 6) due to increased HO₂ availability provided by the new scheme.

Figure 8 also shows that the additional CR-produced NO of scenarios 4.0, 4.1, and 4.3 causes an increased O₃ concentration in the troposphere with regard to scenario 1. The increased availability of NO_x is known to favour the Smog mechanism (see e.g. Haagen-Smit 1952; Grenfell et al. 2006), which is responsible for most tropospherically produced O₃ on Earth.

3.3. Planetary spectra

3.3.1. Emission spectra

We calculate theoretical emission and transmission spectra analogous to Rauer et al. (2011). For exoplanets, planetary emission spectra are best measured close to the secondary transit, where the insolated side of the planet is directed towards the observer. Since it is difficult to separately resolve transiting exoplanets from their host star, therefore the measured flux F_1 is

$$F_1(\lambda) = F_p(\lambda) + F_s(\lambda), \quad (21)$$

where F_p is the planetary emission flux and F_s the stellar flux depending on the wavelength λ . To obtain F_p , another flux has to be measured with $F_2(\lambda) = F_s(\lambda)$, which is realised when the star occults the planet during secondary transit (Rauer et al. 2011). The planetary emission flux is then calculated via

$$F_p(\lambda) = F_1(\lambda) - F_2(\lambda), \quad (22)$$

where F_1 and F_2 need to have the same integration times to remain comparable.

The contrast $C_{p/s}$ between the planetary and stellar spectrum is calculated by

$$C_{p/s}(\lambda) = \frac{F_p(\lambda)}{F_s(\lambda)} = \frac{R_p^2 I_p}{R_s^2 I_s} \quad (23)$$

with the planetary radius R_p , the stellar radius R_s , and the spectral flux densities I_p and I_s of the planet and the star, respectively (Rauer et al. 2011).

Figure 9 shows the planet-to-star contrast $C_{p/s}(\lambda)$ due to emission. We have plotted scenarios 0, 1, 3, and 4, although only scenario 4 shows significant changes with respect to scenario 1. As expected from the chemistry section, the CH₄ signals at 2.3 and 3.4 μm decrease slightly for the flaring scenario (scenario 4), yet they still remain visible because even though 80% of all atmospheric CH₄ is destroyed in the simulated M-star planet for scenario 4, there still remains 50 times more CH₄ than on Earth. Additionally, the O₃ band at 9.6 μm gets weaker, but is still recognizable for the flaring case (scenario 4). An HNO₃

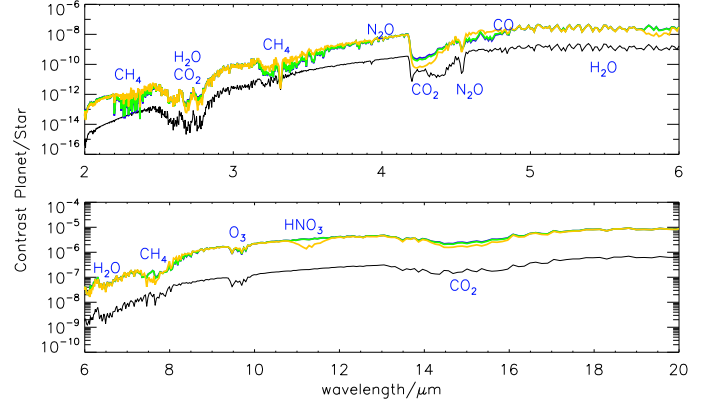


Fig. 9. Planetary emission contrast spectra (with resolution $R = 2000$) for scenarios 0 (Earth GCR: black), 1 (M-dwarf w/o CR: blue), 3 (active M-dwarf: green), and 4 (flaring M-dwarf: yellow). The blue curve is concealed behind the green curve for most wavelengths.

signal becomes visible at around 11.2 μm , consistent with the increased HNO₃ concentration. Spectral signals of CO₂ increase in strength. This is a temperature effect, as a colder stratosphere provides less intensity in the 15 μm CO₂ emission band (see e.g. Takashi 1959).

3.3.2. Transmission spectra

Transmission spectra are obtained through the measurements during and after the primary transit of the planet, where the planet occults a part of the star. In this section theoretical transmission spectra $T_i(\lambda)$ are calculated. Therein we assume that beams cross the atmosphere at equidistant tangent heights corresponding to the atmosphere model layers. The total transmission T is then determined by the sum of individual transmission beams T_i , i.e.

$$T = \frac{1}{H} \sum_i T_i \Delta h_i \quad (24)$$

where Δh_i is the distance between tangent heights and H is the maximum height of the modelled atmosphere.

For the Earth around the Sun a transmission spectrum may lead to higher signal-to-noise in the visible due to its higher stellar flux. M-stars show larger relative fluxes in the IR, which facilitates the study of the absorption bands of relevant chemical species (see Rauer et al. 2011).

Figure 10 shows the relative transmission spectra of the modelled scenarios. For the flaring case (scenario 4), the spectra change considerably, as is expected by the large change in chemical composition presented in the previous section. Spectral signals of CH₄ become weaker compared to the less perturbed cases (see above). The spectral bands of N₂O also become slightly weaker. The ozone band at 9.6 μm remains visible, but is weaker than in the Earth case. This is because, in contrast to Grenfell et al. (2012), not all O₃ is destroyed by NO_x since the HO_x source we introduced provides a sink for NO_x, forming reservoir species such as HNO₃. As a consequence, the spectral signals of HNO₃ become considerably stronger. This suggests that the HNO₃ absorption bands at 11.2 μm may serve as a spectral marker for CRs in Earth-like atmospheres. To confirm this, further study is required regarding the range of possible conditions (UV, NO_x, CR intensity) for which the HNO₃ signal is visible in the theoretical spectra.

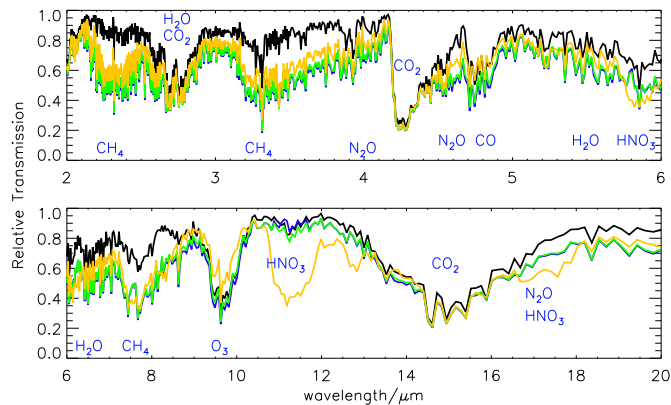


Fig. 10. Relative transmission spectra (with resolution $R = 2000$) for scenarios 0 (Earth GCR: black), 1 (M-dwarf w/o CR: blue), 3 (active M-dwarf: green), and 4 (flaring M-dwarf: yellow). The blue curve is concealed behind the green curve for most wavelengths.

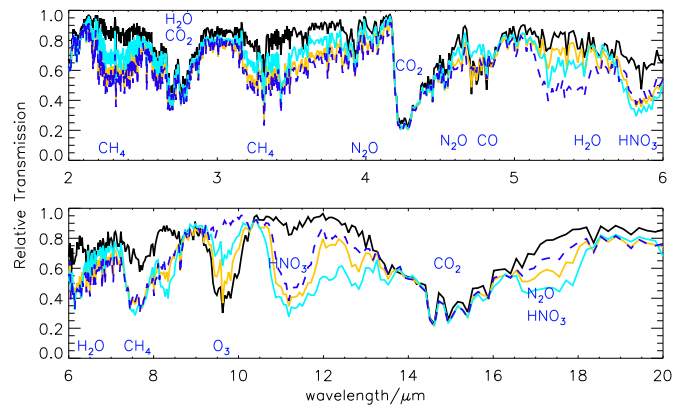


Fig. 12. Relative transmission spectra (with resolution $R = 2000$) for scenarios 0 (Earth GCR: black), 4 (flaring M-dwarf: yellow), 5 (flaring(x40) M-dwarf: light blue), and 6 (flaring M-dwarf(Grenfell et al. 2012): dark blue dashed).

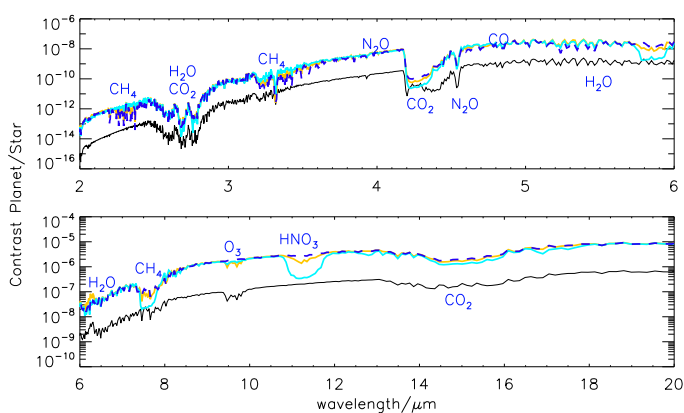


Fig. 11. Planet to star contrast spectra (with resolution $R = 2000$) for scenarios 0 (Earth GCR: black), 4 (flaring M-dwarf: yellow), 5 (flaring(x40) M-dwarf: light blue), and 6 (flaring M-dwarf(Grenfell et al. 2012): dark blue dashed).

3.3.3. The very strongly flaring scenarios

In this section we show planetary spectra for the comparative flaring scenarios (4-6). As mentioned earlier the IPR profile produced by our updated scheme was roughly 40 times smaller than the IPR from our previous scheme (Grenfell et al. 2012). We are confident that our current updates have improved the way we model SCRs. Nevertheless, we not only wish to compare our updated CR scheme directly to our previous one, but also cover the whole spectrum of possible maximum flaring scenarios present in the literature (see e.g. Grenfell et al. 2012) to see how our updated chemistry scheme behaves when fed with these high ion pair production rates.

Figures 11 and 12 show the emission and transmission spectra, respectively, for the flaring scenarios (4-6) as well as the Earth reference case (0). As expected, scenario 6 shows very low O_3 . However, scenario 5 even though it exhibits only 40 DU of tropospheric O_3 , shows a clear O_3 signal in the relative transmission spectra, and a very slight dip in the contrast spectrum. Although somewhat weaker than the O_3 signal of scenario 4, this result shows that for all assumed CR intensities, O_3 remains visible in the theoretical planetary spectra when incorporating CR-induced N and HOx production. Also the HNO_3 signal becomes significantly larger for scenario 5.

4. Surface UV flux

In the previous section, we have seen how SCRs may reduce the atmospheric ozone shield. Now we check whether this reduced ozone shield is still able to efficiently protect the planetary surface against harmful UV radiation.

The UV radiation on the planet's surface could be harmful to developing and existing life. Especially UV-C radiation (for our model 176 - 280 nm) and high doses of UV-B (315 - 280 nm) can damage organic molecules and, thus, be harmful for life.

Similar to Griebmeier et al. (2015b), we numerically study the full UV spectrum from 176 – 315 nm, and present integrated results for the two relevant bands UV-A and UV-B. The UV-C fluxes turn out to be negligible as a result of the efficiency of atmospheric shielding in this wavelength range.

4.1. Surface flux calculation

Here, we give a brief description of the way we calculate the surface UV flux. More details can be found in Griebmeier et al. (2015b).

- We take the wavelength-resolved stellar UV flux and, with the planetary orbital distance, calculate the flux incident at TOA of the M-dwarf star planet. From this we calculate the wavelength-integrated TOA UV fluxes I_{TOA}^{UV-A} and I_{TOA}^{UV-B} .
- For this UV flux, using the numerical model described in Sect. 2.2, we calculate the wavelength-resolved flux of UV at the planetary surface. From this, we calculate the wavelength-integrated surface UV fluxes $I_{surface}^{UV-A}$ and $I_{surface}^{UV-B}$.
- We calculate the ratio of UV penetrating through the planetary atmosphere, averaged over the corresponding UV band, i.e. $R^{UV-A} = I_{surface}^{UV-A} / I_{TOA}^{UV-A}$ and $R^{UV-B} = I_{surface}^{UV-B} / I_{TOA}^{UV-B}$. Thus, R characterised the average UV shielding by the atmosphere in a particular wavelength band.
- We multiply the wavelength-resolved UV surface spectra with the DNA action spectrum of Cuntz et al. (2009, Fig. 1) to calculate the effective biological UV flux W at the planetary surface. In this, the DNA action spectrum is normalised to 1 at a wavelength of 300 nm.

We examine the UV flux for the main scenarios from Sect. 2.1: scenarios 1 (M-dwarf w/o CR), 2 (quiescent M-dwarf), 3 (active M-dwarf), and 4 (flaring M-dwarf). In addition, we compare these scenarios to a scenario with Galac-

tic (rather than stellar) cosmic rays, taking the results from Grießmeier et al. (2015b). For all cases discussed in this section, we assume unmagnetised planets, following the argumentation of Grießmeier et al. (2015a) and Grießmeier et al. (2015b) that magnetic fields on super-Earths around M-dwarf stars are likely to be weak and short-lived.

For each of these scenarios, we examine three different cases for the UV flux: quiescent UV (as is assumed throughout the rest of this article), short UV flare, and long UV flare:

- Quiescent UV: We use the TOA UV spectrum of AD Leonis, as described in Sect. 2.2.
- Short UV flare: During a stellar flare, the UV flux increases by one order of magnitude in a typical case, and by at least two orders of magnitude in more extreme cases with a timescale of 10^2 - 10^3 seconds. We use the TOA UV spectrum of Segura et al. (2010, Fig. 3, bold blue line, scaled for distance), i.e. the maximum flux at the flare peak. Our model does not feature time dependence. Therefore, if the timescale of the UV flare (e.g. its duration) is short compared to the atmospheric reaction time, we assume that the atmosphere has not yet adjusted to the increased UV flux. In this case, we use the atmospheric transfer function $R(\lambda)$ obtained in the quiescent UV case, and multiply this function with the TOA flare UV flux. This scenario is appropriate for an isolated flare.
- Long UV flare: The flare timescale is longer than the typical reaction time of the planetary atmosphere where it is assumed that the atmosphere is continuously perturbed. In this case, we calculate the surface UV flux using the flare TOA flux via the model of Sect. 2.2. This scenario is appropriate for quasi-continuous flares.

4.2. Surface flux results

Tables 5, 6, and 7 show the UV-A flux (315-400nm), the UV-B flux (280-315 nm), and the biologically weighted UV-flux W for scenarios 1 through 4 plus, for comparison, the Galactic cosmic ray scenario from Grießmeier et al. (2015b). For each scenario, we also compare the three different UV cases discussed above.

As seen in Table 5, the atmospheric transmission coefficient R for UV-A is virtually independent of the cosmic ray environment. It does, however, vary with the ambient UV conditions. During a long UV-flare, the surface receives up to 50 times more UV-A radiation than under quiescent conditions.

Table 6 shows that the UV-B flux is more sensitive to the destruction of the ozone layer by CRs. The presence of a strong cosmic ray environment can increase the atmospheric transmission coefficient for UV-B (and the surface UV-B flux) by a factor of almost 4. Still, the variability of the surface UV flux is dominated by the UV activity of the host star, which can change the surface UV-B flux by over two orders of magnitude.

The biological radiation damage created by UV-A radiation is several orders of magnitude weaker than the damage caused by UV-B radiation (e.g. Cuntz et al. 2009). Thus, it is not surprising to see that the biologically weighted UV flux W qualitatively shows a similar behaviour as the UV-B flux. Quantitatively, the response of W is stronger than that of the average UV-B flux. This results from the fact that W is sensitive mostly to UV-B flux at 300 nm, which is more variable than the band-averaged UV-B flux. Table 7 shows that under high cosmic ray fluxes (i.e. during a strong stellar particle flare), the planetary ozone shield is reduced strongly enough to increase the weighted surface UV flux W by a factor of 20. During a long stellar UV-flare, W increased by an additional factor of 100. When compared to

Earth, the value of W remains below the terrestrial value for almost all cases. However, when the high UV flux of a long stellar flare coincides with a stellar particle eruption (which reduces the atmospheric UV shield), W reaches values considerably higher than on present day Earth (40 times the present-day terrestrial value).

Our results compare well to previous work, and extend them by including the increase in stellar UV flux. Grenfell et al. (2012) consider the effect of the particle flux on the atmospheric ozone layer, but do not take the increase in stellar UV during a flare into account. Grenfell et al. (2012) find that the surface flux of UV-B (their Table 2) is increased by a factor of ~ 30 in the flaring case. Even with this, the surface UV-B flux is considerably lower than the terrestrial value, which is qualitatively consistent with our quiescent UV case. In the current work (using the new modelling scheme), less ozone is destroyed by SCRs, so that the surface is better protected against UV-B. However, in the new cases of stellar UV flares (both short and long), this is more than compensated by the increase in stellar UV flux, leading to an increase in surface UV-B by several orders of magnitude.

Our results are also compatible with those of Segura et al. (2010). They considered both the flare's increased UV radiation and a proton event at the peak of the flare. Their flare peak is comparable to our short UV-flare case for the flaring M-dwarf scenario (see their Table 2), and the UV-B surface flux values are indeed comparable. Our work adds the long UV-flare case, which has a higher potential impact on habitability, and the analysis of the biologically weighted surface UV flux.

4.3. Surface flux: Discussion

Our main findings are as follows. We find that CRs leave the UV-A transmission coefficient and flux virtually unchanged. For UV-B, GCRs modify the transmission rate and surface flux by less than 20%, whereas SCRs change R by more than a factor of two. For the GCR scenario, short flares are more harmful than long flares. For the SCR scenarios, long flares (where R has time to adjust to the modified particle flux) are more harmful than short flares.

Regarding the biologically weighted UV surface flux W , GCRs can change W by up to 40%, while SCRs can change W by over one order of magnitude. In all cases, W is dominated by the contribution of UV-B. In the case of Earth (without any CRs), $W = 0.125 \text{ W/m}^2$ (Grießmeier et al. 2015b). Except in the long UV flare case, the corresponding value for an M-dwarf, even when subject to strong cosmic ray fluxes, is lower. With $W \leq 4.9 \text{ W/m}^2$ (Table 7), the SCR-induced surface UV radiation during a long stellar UV flare may indeed potentially be harmful for certain types of cells (e.g. human skin or eye cells), but is not strong enough to prevent life. For example, *Deinococcus radiodurans* is able to withstand a flux of $> 40 \text{ W/m}^2$ without significant damage, and life on Earth may have arisen during times when the biologically weighted UV flux was even higher ($> 96 \text{ W/m}^2$, see Cockell 1999).

5. Discussion

In the context of the photochemistry of Earth-like atmospheres the unconstrained parameter range is large. Key parameters include atmospheric pressure (e.g. Vladilo et al. 2013), composition (e.g. Segura et al. 2007), incoming stellar spectrum (e.g. Segura et al. 2003), position in the habitable zone (e.g. Grenfell et al. 2007b), incoming cosmic ray fluxes (e.g.

case #	UV-A	quiescent UV			short UV flare			long UV flare		
		$I_{\text{TOA}}^{\text{UV-A}}$ [W/m ²]	$I_{\text{surface}}^{\text{UV-A}}$ [W/m ²]	$R^{\text{UV-A}}$	$I_{\text{TOA}}^{\text{UV-A}}$ [W/m ²]	$I_{\text{surface}}^{\text{UV-A}}$ [W/m ²]	$R^{\text{UV-A}}$	$I_{\text{TOA}}^{\text{UV-A}}$ [W/m ²]	$I_{\text{surface}}^{\text{UV-A}}$ [W/m ²]	$R^{\text{UV-A}}$
1	M-dwarf w/o CR	2.1	1.5	0.72	82	57	0.69	82	76	0.92
*	GCR	2.1	1.5	0.72	82	57	0.69	82	76	0.92
2	SCR (quiescent M dwarf)	2.1	1.5	0.72	82	57	0.69	82	76	0.92
3	SCR (active M dwarf)	2.1	1.5	0.72	82	57	0.69	82	76	0.92
4	SCR (flaring M dwarf)	2.1	1.5	0.72	82	56	0.69	82	79	0.97

Table 5. UV-A flux at top of atmosphere ($I_{\text{TOA}}^{\text{UV-A}}$), at the surface ($I_{\text{surface}}^{\text{UV-A}}$), and wavelength-range averaged atmospheric transmission coefficient $R^{\text{UV-A}} = I_{\text{surface}}^{\text{UV-A}} / I_{\text{TOA}}^{\text{UV-A}}$. Notes: * results taken from Grießmeier et al. (2015b, their cases CA, LF and SF, each with $M = 0$).

case #	UV-B	quiescent UV			short UV flare			long UV flare		
		$I_{\text{TOA}}^{\text{UV-B}}$ [W/m ²]	$I_{\text{surface}}^{\text{UV-B}}$ [W/m ²]	$R^{\text{UV-B}}$	$I_{\text{TOA}}^{\text{UV-B}}$ [W/m ²]	$I_{\text{surface}}^{\text{UV-B}}$ [W/m ²]	$R^{\text{UV-B}}$	$I_{\text{TOA}}^{\text{UV-B}}$ [W/m ²]	$I_{\text{surface}}^{\text{UV-B}}$ [W/m ²]	$R^{\text{UV-B}}$
1	M-dwarf w/o CR	0.18	0.020	0.11	49	4.8	0.10	49	3.1	0.06
*	GCR	0.18	0.023	0.13	49	5.3	0.11	49	3.1	0.06
2	SCR (quiescent M dwarf)	0.18	0.021	0.12	49	4.8	0.10	49	3.1	0.06
3	SCR (active M dwarf)	0.18	0.028	0.16	49	4.8	0.10	49	3.1	0.06
4	SCR (flaring M dwarf)	0.18	0.05	0.28	49	4.8	0.10	49	11.4	0.23

Table 6. As table 5, but for UV-B.

case #	biologically weighted surface flux W [W/m ²] (compared to Present Day Earth)	quiescent UV	short UV flare	long UV flare
1	M-dwarf w/o CR	0.0015 (0.01 PDE [†])	0.48 (4 PDE [†])	0.15 (1.2 PDE [†])
*	GCR	0.0021 (0.02 PDE [†])	0.61 (5 PDE [†])	0.15 (1.2 PDE [†])
2	SCR (quiescent M dwarf)	0.0017 (0.01 PDE [†])	0.48 (0.01 PDE [†])	0.15 (1.2 PDE [†])
3	SCR (active M dwarf)	0.15 (1.2 PDE [†])	0.48 (0.01 PDE [†])	0.17 (1.3 PDE [†])
4	SCR (flaring M dwarf)	0.025 (0.2 PDE [†])	0.48 (0.01 PDE [†])	4.9 (40 PDE [†])

Table 7. Biologically weighted surface UV-flux, in weighted W/m² and relative to present day Earth. Notes: * results taken from Grießmeier et al. (2015b, their cases CA, LF and SF, each with $M = 0$). [†] PDE=Present Day Earth ($W=0.126$ W/m², see Grießmeier et al. (2015b))

Grießmeier et al. 2015a). Our model results can be compared best to the work of Grenfell et al. (2012) as we use the same radiative-convective/photochemical model, but with an improved CR scheme (see Sect. 2.3). A comparison shows that the improved scheme conserves spectrally visible amounts of O₃ in the studied atmospheres and catalytic O₃ destruction is partly mitigated, helped also by an NO_x-induced O₃-producing smog mechanism in the troposphere. Another application of a photochemical model to exoplanets includes a study by Segura et al. (2005), who studied the effect of an M-dwarf spectrum on an Earth-like atmosphere. Their placement of the planet within the HZ differs from the current work in that their total stellar flux was normalised so that the surface temperature equals 288 K. Segura et al. (2005) find large concentrations of CH₄ (Earth-like biogenic flux, but decreased photolysis of CH₄), causing a strong CH₄ greenhouse effect. Adding CR-induced OH production to our scheme provides a further sink for the high CH₄ levels. This causes a reduction of CH₄ concentrations by a factor of five in the flaring case (4) as well as a reduction in the surface temperature by 7 K. Segura et al. (2010) have studied the effect of an M-dwarf stellar flare. As mentioned in section 4.2 the UV-B

values of our short UV-flare case for the flaring M-dwarf scenario and their flare peak are comparable. Further photochemical studies regarding planets orbiting M-dwarf planets include Tian et al. (2014), who use an early-Earth model with variable O₂ and high CO₂ concentrations, whereas we assume an Earth-like setup with constant N₂, O₂, CO₂ and biogenic fluxes. While Tian et al. (2014) study the abundance of O₂ under abiotic conditions for different CO₂ mixing ratios, we study the effect of (in this case) CRs on bioindicator species and trace gases under biotic and Earth-like conditions. Additionally, Tian et al. (2014) use the stellar spectrum of an M-dwarf with low UV flux due to recent measurements of quiescent M-dwarfs (France et al. 2012, 2013), whereas we use the active M-dwarf spectrum of AD Leo to provide comparison to previous works and because the current work focuses on the influence of the changes to the CR scheme. The impact of different M-dwarf spectra to our photochemical model was studied by Grenfell et al. (2013, 2014). Grenfell et al. (2013) presented a detailed analysis of atmospheric pathways that form and destroy, e.g. O₃, for an Earth-like planet orbiting in the HZ of different M-dwarf stars. Grenfell et al. (2014) studied the effect of varying the (uncertain) incoming UV flux for Earth-

like planets orbiting in the HZ of M-dwarfs. They found that while increases in $UV_{200-300\text{nm}}$ favoured O_3 loss via photolysis, increases in $UV_{<200\text{nm}}$ favoured O_3 production by stimulating O_2 photolysis.

Several caveats of our model require discussion. The parametrisations used in the chemistry improvements were set up for the Earth atmosphere only, and are hence valid when assuming a nitrogen-oxygen dominated atmosphere with Earth's mixing ratios. Calculating other atmospheric compositions would require input from an ion chemistry model to infer IPR as well as production coefficients.

The changes to our air-shower scheme have caused the IPR of our constant flaring scenario to decrease by a factor of 40. However, these changes have made our model more physically realistic, as primary particles of different energies now produce decidedly different amounts of secondary electrons at different altitudes, which was only partially true for the old scheme. In addition, we have shown that the changes to our chemical scheme with regard to CRs lead to less photochemical O_3 loss, so that this species is then visible in the theoretical spectra, even for an IPR increased by a factor of 40 (see Sect. 3.3.3).

It is challenging to apply our CR air-shower scheme to the relatively low energies of primary proton fluxes originating from the planet's host star (SCRs). We need better information on ion pair production rates for low-energy cosmic ray particles are, to better constrain the interpolation from higher to lower energies.

Our atmospheric model operates in steady state. Consequently, time-resolved flaring scenarios are not possible. Nevertheless, for strongly flaring stars such as AD Leo, we generally assume rapid flaring compared to photochemical response timescale suggesting a (quasi-)stationarity. Since such a constant flare output would in reality still vary largely in intensity, our constant flaring scenario is therefore to be considered as an upper boundary of the possible effect of SCRs on the atmospheric chemistry of Earth-like planets in the HZ of flaring M-dwarfs.

6. Summary and conclusion

We improved upon the CR scheme of Grenfell et al. (2012) by updating the CR parametrisation parameters, as well as adding CR-induced production of N and HOx to the existing NO production scheme via ion pair production parametrisations obtained from Earth measurements by Jackman et al. (1980) and Solomon et al. (1981). With these improvements, we have shown that the atmospheric effects of high CR fluxes do not completely destroy O_3 reservoirs as previously calculated (see Grenfell et al. 2012), but leave enough O_3 such that it remains visible in theoretical planetary spectra. The atmospheric accumulation of CR-produced NOx and HOx leads to a very large HNO_3 reservoir, whose signal is very clear in the theoretical spectra.

Our main results are that SCR-induced NOx and HOx production for Earth-like planets orbiting in the HZ of M-dwarfs removes some of the produced NO via storage as HNO_3 , thereby weakening the catalytic destruction of O_3 . We find that HNO_3 may be a potentially detectable indicator of high incident stellar particle flux, yet further investigation is needed. Additionally, the new CR chemistry scheme helps destroy significant amounts of CH_4 due to increased OH production. Both O_3 and CH_4 remain visible in the modelled planetary spectra even when assuming a constant flaring of the host star.

If a stellar cosmic ray particle event coincides with a stellar UV flare, the surface UV flux may strongly exceed that of present-day Earth. This flux level exceeds that found previously

(Grießmeier et al. 2015b) for the case of GCRs. Still, even if the SCR-induced surface UV radiation may indeed be potentially harmful for certain types of cells, it is not strong enough to prevent life.

References

- Alvarez-Muniz, J., Engel, R., Gaisser, T., Ortiz, J. A., & Stanev, T. 2002, *Physical Review D*, 66, 033011
- Calisto, M., Usoskin, I., Rozanov, E., & Peter, T. 2011, *Atmospheric Chemistry and Physics*, 11, 4547
- Cockell, C. S. 1999, *Icarus*, 141, 399
- COESA (U.S. Committee on Extension to the Standard Atmosphere). 1976, US standard atmosphere, 1976, Tech. rep.
- Cuntz, M., Guinan, E. F., & Kurucz, R. L. 2009, *Solar and Stellar Variability: Impact on Earth and Planets*, IAU Symposium 264, eds. A. G. Kosovichev, A. H. Andrei, and J.-P. Rozelot, 5, 419
- Des Marais, D. J., Harwit, M. O., Jucks, K. W., et al. 2002, *Astrobiology*, 2, 153
- Dressing, C. D., Spiegel, D. S., Scharf, C. A., Menou, K., & Raymond, S. N. 2010, *The Astrophysical Journal*, 721, 1295
- Ehrenreich, D., Tinetti, G., Des Etangs, A. L., Vidal-Madjar, A., & Selsis, F. 2006, *Astronomy & Astrophysics*, 448, 379
- France, K., Froning, C. S., Linsky, J. L., et al. 2013, *The Astrophysical Journal*, 763, 149
- France, K., Linsky, J. L., Tian, F., Froning, C. S., & Roberge, A. 2012, *The Astrophysical Journal Letters*, 750, L32
- Gaisser, T. K. & Hillas, A. M. 1977, in *International Cosmic Ray Conference*, Vol. 8, 353–357
- Godolt, M. 2012, PhD thesis, Universitätsbibliothek der Technischen Universität Berlin
- Grenfell, J., Gebauer, S., Godolt, M., et al. 2013, *Astrobiology*, 13, 415
- Grenfell, J., Gebauer, S., Paris, P. v., Godolt, M., & Rauer, H. 2014, *Planetary and Space Science*, 98, 66
- Grenfell, J. L., Gebauer, S., Von Paris, P., et al. 2011, *Icarus*, 211, 81
- Grenfell, J. L., Grießmeier, J.-M., Patzer, B., et al. 2007a, *Astrobiology*, 7, 208
- Grenfell, J. L., Grießmeier, J.-M., von Paris, P., et al. 2012, *Astrobiology*, 12, 1109
- Grenfell, J. L., Stracke, B., Patzer, B., Titz, R., & Rauer, H. 2006, *International Journal of Astrobiology*, 5, 295
- Grenfell, J. L., Stracke, B., von Paris, P., et al. 2007b, *Planetary and Space Science*, 55, 661
- Grießmeier, J.-M., Stadelmann, A., Grenfell, J., Lammer, H., & Motschmann, U. 2009, *Icarus*, 199, 526
- Grießmeier, J.-M., Stadelmann, A., Motschmann, U., et al. 2005, *Astrobiology*, 5, 587
- Grießmeier, J.-M., Tabataba-Vakili, F., Stadelmann, A., Grenfell, J., & Atri, D. 2015a, *Astronomy & Astrophysics*, 581, A44
- Grießmeier, J.-M., Tabataba-Vakili, F., Stadelmann, A., Grenfell, J. L., & Atri, D. 2015b, *Astronomy & Astrophysics*, submitted
- Gueymard, C. A. 2004, *Solar energy*, 76, 423
- Haagen-Smit, A. 1952, *Industrial & Engineering Chemistry*, 44, 1342
- Hauschildt, P. H., Allard, F., & Baron, E. 1999, *The Astrophysical Journal*, 512, 377
- Huang, S.-S. 1959, *American scientist*, 47, 397
- Ingersoll, A. P. 1969, *Journal of the atmospheric sciences*, 26, 1191
- Itikawa, Y. 2006, *Journal of physical and chemical reference data*, 35, 31
- Jackman, C., Frederick, J., & Stolarski, R. 1980, *Journal of Geophysical Research: Oceans (1978–2012)*, 85, 7495
- Jackman, C. H., DeLand, M. T., Labow, G. J., et al. 2005, *Journal of Geophysical Research: Space Physics (1978–2012)*, 110
- Jackman, C. H., Douglass, A. R., Rood, R. B., McPeters, R. D., & Meade, P. E. 1990, *Journal of Geophysical Research: Atmospheres (1984–2012)*, 95, 7417
- Joshi, M. 2003, *Astrobiology*, 3, 415
- Kaltenegger, L. & Sasselov, D. 2010, *The Astrophysical Journal*, 708, 1162
- Kaltenegger, L. & Traub, W. A. 2009, *The Astrophysical Journal*, 698, 519
- Kaltenegger, L., Traub, W. A., & Jucks, K. W. 2007, *The Astrophysical Journal*, 658, 598
- Kasting, J. F. 1988, *Icarus*, 74, 472
- Kasting, J. F., Holland, H. D., & Pinto, J. P. 1985, *Journal of Geophysical Research: Atmospheres (1984–2012)*, 90, 10497
- Kasting, J. F., Pollack, J. B., & Crisp, D. 1984, *Journal of atmospheric chemistry*, 1, 403
- Kasting, J. F., Whitmire, D. P., & Reynolds, R. T. 1993, *Icarus*, 101, 108
- Khodachenko, M., Alexeev, I., Belenkaya, E., et al. 2012, *The Astrophysical Journal*, 744, 70
- Kuznetsov, N., Nymmik, R., & Panasyuk, M. 2005, *Advances in Space Research*, 36, 2003

- Lammer, H., Lichtenegger, H., Khodachenko, M., Kulikov, Y. N., & Griessmeier, J.-M. 2011, in *Astronomical Society of the Pacific Conference Series*, Vol. 450, 139
- Leggett, S., Allard, F., Berriman, G., Dahn, C. C., & Hauschildt, P. H. 1996, *The Astrophysical Journal Supplement Series*, 104, 117
- Manabe, S. & Wetherald, R. T. 1967
- Massie, S. & Hunten, D. 1981, *Journal of Geophysical Research: Oceans* (1978–2012), 86, 9859
- Mayor, M. & Queloz, D. 1995, *Nature*, 378, 355
- Mlawer, E. J., Taubman, S. J., Brown, P. D., Iacono, M. J., & Clough, S. A. 1997, *Journal of geophysical research*, 102, 16663
- Nicolet, M. 1975, *Planetary and Space Science*, 23, 637
- NIST. 2013, *Cross Section Molecule Information*
- Pettersen, B. & Hawley, S. 1989, *Astronomy and Astrophysics*, 217, 187
- Pfotzer, G. 1936, *Zeitschrift für Physik*, 102, 23
- Porter, H., Jackman, C., & Green, A. 1976, *The Journal of Chemical Physics*, 65, 154
- Rauer, H., Gebauer, S., Paris, P. v., et al. 2011, *Astronomy & Astrophysics*, 529
- Rauscher, E. & Menou, K. 2012, *The Astrophysical Journal*, 745, 78
- Rothman, L. S., Jacquemart, D., Barbe, A., et al. 2005, *Journal of Quantitative Spectroscopy and Radiative Transfer*, 96, 139
- Sander, S., Friedl, R., Ravishankara, A., et al. 2003
- Scalo, J., Kaltenecker, L., Segura, A., et al. 2007, *Astrobiology*, 7, 85
- Schreier, F. & Böttger, U. 2003, *Atmospheric and Oceanic Optics c/c of Optika Atmosfery i Okeana*, 16, 262
- Schreier, F. & Schimpf, B. 2001, *IRS 2000: Current Problems in Atmospheric Radiation*
- Segura, A., Kasting, J. F., Meadows, V., et al. 2005, *Astrobiology*, 5, 706
- Segura, A., Krelow, K., Kasting, J. F., et al. 2003, *Astrobiology*, 3, 689
- Segura, A., Meadows, V., Kasting, J., Crisp, D., & Cohen, M. 2007, *Astronomy & Astrophysics*, 472, 665
- Segura, A., Walkowicz, L. M., Meadows, V., Kasting, J., & Hawley, S. 2010, *Astrobiology*, 10, 751
- Selsis, F. 2000, in *Darwin and Astronomy: the Infrared Space Interferometer*, Vol. 451, 133
- Selsis, F., Despois, D., & Parisot, J.-P. 2002, *Astronomy & Astrophysics*, 388, 985
- Sen, B., Toon, G., Osterman, G., et al. 1998, *Journal of Geophysical Research: Atmospheres* (1984–2012), 103, 3571
- Seo, E., McDonald, F., Lal, N., & Webber, W. 1994, *The Astrophysical Journal*, 432, 656
- Sinnhuber, M., Nieder, H., & Wieters, N. 2012, *Surveys in Geophysics*, 33, 1281
- Smart, D. & Shea, M. 2002, *Advances in Space Research*, 30, 1033
- Solomon, S., Rusch, D., Gérard, J.-C., Reid, G., & Crutzen, P. 1981, *Planetary and Space Science*, 29, 885
- Spiegel, D. S., Menou, K., & Scharf, C. A. 2009, *The Astrophysical Journal*, 691, 596
- Sworzy, S. & Kieda, D. 2000, *Astroparticle Physics*, 13, 137
- Takashi, S. 1959
- Tessenyi, M., Tinetti, G., Savini, G., & Pascale, E. 2013, *Icarus*, 226, 1654
- Tian, F., France, K., Linsky, J. L., Mauas, P. J., & Vieytes, M. C. 2014, *Earth and Planetary Science Letters*, 385, 22
- Tinetti, G., Meadows, V. S., Crisp, D., et al. 2006, *Astrobiology*, 6, 881
- Toon, O. B., McKay, C., Ackerman, T., & Santhanam, K. 1989, *Journal of Geophysical Research: Atmospheres* (1984–2012), 94, 16287
- Usoskin, I. G., Desorgher, L., Velinov, P., et al. 2009, *Acta Geophysica*, 57, 88
- Velinov, P. & Mateev, L. 2008, *Journal of Atmospheric and Solar-Terrestrial Physics*, 70, 574
- Verronen, P. & Lehmann, R. 2013, *Annales Geophysicae*, 31, 909
- Vidotto, A., Fares, R., Jardine, M., Moutou, C., & Donati, J.-F. 2015, *arXiv preprint arXiv:1503.05711*
- Vidotto, A., Jardine, M., Morin, J., et al. 2013, *Astronomy & Astrophysics*, 557, A67
- Vladilo, G., Murante, G., Silva, L., et al. 2013, *The Astrophysical Journal*, 767, 65
- Winkler, H., Sinnhuber, M., Notholt, J., et al. 2008, *Journal of Geophysical Research: Atmospheres* (1984–2012), 113
- Wissing, J. & Kallenrode, M.-B. 2009, *Journal of Geophysical Research: Space Physics* (1978–2012), 114
- Yang, J., Cowan, N. B., & Abbot, D. S. 2013, *The Astrophysical Journal Letters*, 771, L45

